ICES Journal of Marine Science Advance Access published October 29, 2009

Measurements of acoustic scattering from zooplankton and oceanic microstructure using a broadband echosounder

Andone C. Lavery, Dezhang Chu, and James N. Moum

Lavery, A. C., Chu, D., and Moum, J. N. 2010. Measurements of acoustic scattering from zooplankton and oceanic microstructure using a broadband echosounder. – ICES Journal of Marine Science, 67: 000–000.

In principle, measurements of high-frequency acoustic scattering from oceanic microstructure and zooplankton across a broad range of frequencies can reduce the ambiguities typically associated with the interpretation of acoustic scattering at a single frequency or a limited number of discrete narrowband frequencies. With this motivation, a high-frequency broadband scattering system has been developed for investigating zooplankton and microstructure, involving custom modifications of a commercially available system, with almost complete acoustic coverage spanning the frequency range 150–600 kHz. This frequency range spans the Rayleigh-to-geometric scattering transition for some zooplankton, as well as the diffusive roll-off in the spectrum for scattering from turbulent temperature microstructure. The system has been used to measure scattering from zooplankton and microstructure in regions of non-linear internal waves. The broadband capabilities of the system provide a continuous frequency response of the scattering over a wide frequency band, and improved range resolution and signal-to-noise ratios through pulse-compression signal-processing techniques. System specifications and calibration procedures are outlined and the system performance is assessed. The results point to the utility of high-frequency broadband scattering techniques in the detection, classification, and under certain circumstances, quantification of zooplankton and microstructure.

Keywords: broadband acoustic scattering, internal waves, oceanic microstructure, zooplankton.

Received 18 February 2009; accepted 9 September 2009.

A. C. Lavery and D. Chu: Department of Applied Ocean Physics and Engineering, Woods Hole Oceanographic Institution, Woods Hole, MA 02543-1053, USA. D. Chu: NOAA/NMFS/NWFSC, 2725 Montlake Boulevard East, Seattle, WA 98112, USA. J. N. Moum: College of Oceanic and Atmospheric Sciences, Oregon State University, 104 COAS Admin Building, Corvallis, OR 97331-5503, USA. Correspondence to A. C. Lavery: tel: +1 508 289 2345; fax: +1 508 457 2194; e-mail: alavery@whoi.edu.

Introduction

Over the past 40 years, significant research effort has been directed at using high-frequency scattering techniques to investigate remotely the distribution, abundance, and size of marine organisms (Simmonds and MacLennan, 2005, and references therein). More recently, there has also been significant effort directed towards the quantitative use of scattering techniques for investigating small-scale physical processes, such as oceanic microstructure (e.g. Goodman, 1990; Seim *et al.*, 1995; Lavery *et al.*, 2003; Ross and Lueck, 2003; Warren *et al.*, 2003). Scattering techniques provide a rapid, high-resolution, synoptic, remote-sensing alternative to more traditional sampling strategies. However, reducing the ambiguities in the quantitative interpretation of the acoustic returns, with the goal of accurate, remote classification and quantification of physical and/or biological scattering sources, remains one of the challenges outstanding.

An important factor contributing to the ambiguities in accurately interpreting scattering data is the wide variety of scattering sources of both biological (including fish, squid, and zooplankton) and physical (microstructure, bubbles, and suspended sediments) origin. Further exacerbating the accurate interpretation of acoustic data is the fact that many of these scattering sources occur simultaneously, e.g. mixed zooplankton assemblages in which the individual constituents have different scattering characteristics (Lavery *et al.*, 2007), or turbulence patches in which small zooplankton or bubbles can act as passive tracers of the underling turbulence. Moreover, many of these physical and biological sources of scattering are patchy and intermittent across a broad range of spatial and temporal scales and can occur simultaneously (Rothschild and Osborn, 1988; Seuront *et al.*, 2001; Ross *et al.*, 2007). It has also been suggested that biological organism themselves can generate acoustically measurable levels of turbulence (Huntley and Zhou, 2004; Kunze *et al.*, 2006).

Understanding the scattering from any one source can be challenging because the frequency-dependent scattering depends on a number of parameters, many of which are difficult to quantify by any sampling technique, particularly *in situ*. For example, the scattering of sound from zooplankton depends in a complicated way on the three-dimensional variations in the material properties (i.e. the sound speed and density throughout the organism), the shape and size, and the orientation relative to the incident acoustic wave (Stanton *et al.*, 1998a, b). The scattering of sound from oceanic microstructure depends on parameters such as the temperature and salinity gradients, the dissipation rate of turbulent kinetic energy, and the degree of anisotropy (Goodman, 1990; Seim *et al.*, 1995; Lavery *et al.*, 2003; Leong, 2009).

The development of high-frequency broadband scattering techniques, spanning multiple octaves of bandwidth, may in principle

lead to decreases in the ambiguities associated with interpretation of scattering measurements of zooplankton and microstructure. The goal is to capitalize on the different characteristic frequency-dependent spectra associated with different scattering sources. Measurements of high-frequency acoustic scattering from zooplankton and microstructure are typically performed at a restricted number, typically 1–4, narrowband frequencies (Holliday and Pieper, 1995; Wiebe *et al.*, 1997; Trevorrow *et al.*, 2005). Some of the world's largest stocks of zooplankton, such as Antarctic krill (*Euphausia superba*; Nicol and Endo, 1999), are assessed using single or multifrequency narrowband scattering techniques (Simmonds and MacLennan, 2005). However, the use of a limited number of narrowband frequencies can lead to inadequate mapping of the scattering spectra. By measuring the scattering spectra continuously over a range of frequencies, there is the potential, in principle, to optimize the classification and quantification accuracy. The potential for this technique is supported by laboratory measurements of broadband scattering from zooplankton (Stanton *et al.*, 1998a; Roberts and Jaffe, 2008), micronekton (Au and Benoit-Bird, 2008), and different types of microstructure (Stanton *et al.*, 1994; Oeschger and Goodman, 2003; Lavery and Ross, 2007), as well as the fact that many toothed whales use broadband echolocation signals to detect and classify their prey (Au *et al.*, 2009). Note that a sufficiently large number of narrowband frequencies, such as the 21-frequency Multi-frequency Acoustic Profiling System (Pieper *et al.*, 1990; Napp *et al.*, 1993), developed for zooplankton applications and spanning the frequency range 100 kHz to many MHz can achieve similar results as broadband measurements in terms of optimizing spectral coverage. However, such an approach cannot capitalize on the high spatial resolution associated with broadband signal processing.

There are only a few commercially available (Ross and Lawson, 2009: 85–155 kHz), or custom-built prototype (Foote *et al.*, 2005: 25 kHz to 3.2 MHz), high-frequency broadband scattering systems that have been used for studying zooplankton and microstructure in the field. In contrast, lower frequency broadband scattering measurements ($<\sim$120 kHz) to characterize fish remotely have been performed more prevalently (Zakharia *et al.*, 1996; Stanton *et al.*, 2010), including measurements involving explosives (Holliday, 1972; Thompson and Love, 1996).

Relatively straightforward modifications to a commercially available sidescan sonar system developed by EdgeTech, Inc. (1141 Holland Drive, Bay 1, Boca Raton Branch, FL, USA) are described here, and they have allowed high-frequency broadband scattering measurements to be performed almost continuously over the frequency range 150–600 kHz. This frequency range encompasses many of the narrowband acoustic frequencies typically used to survey zooplankton and oceanic microstructure. It also includes the Rayleigh-to-geometric scattering transition of some zooplankton and the diffusive roll-off (referring to the rapid decrease in scattering with increasing frequency) in the spectrum for scattering from turbulent temperature microstructure (Figure 1).

The broadband system uses pulse-compression signal-processing techniques that are closely related to matched filter processing, both commonly used techniques in radar and sonar applications (Turin, 1960; Van Trees, 1968; Whalen, 1971). These techniques have been adapted successfully to the zooplankton and fish-scattering problem by Chu and Stanton (1998) and Stanton and Chu (2008). One of the advantages of pulse-compression processing of broadband signals is increased

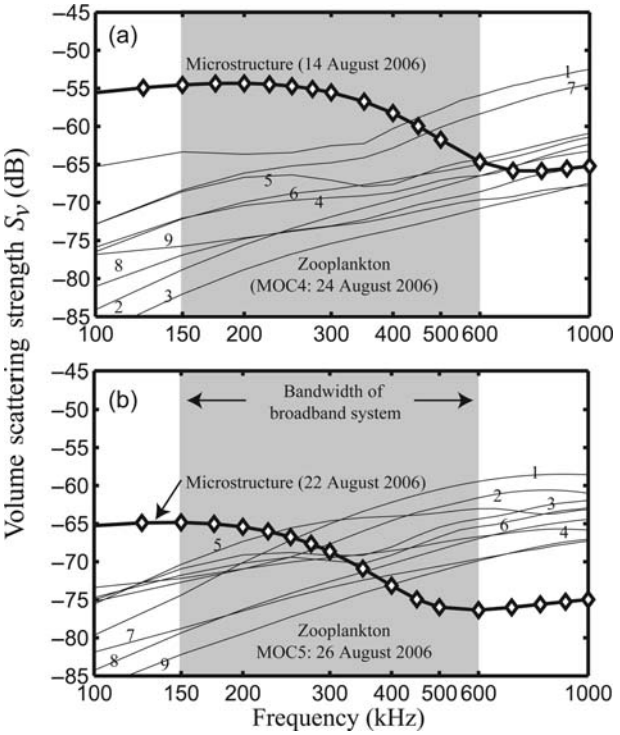

Figure 1. Total predicted volume backscattering strength, S_v (dB), as a function of frequency and net number (thin contour lines labelled 1 through 9) for the zooplankton net tows performed on (a) 24 August 2006 and (b) 26 August 2006. Predicted volume backscattering strengths for turbulent microstructure (indicated by thick lines with diamonds) correspond to predictions based on the inversions for the non-linear internal waves imaged on (a) 14 August 2006 and (b) 22 August 2006. The bandwidth of the EdgeTech broadband scattering system is shown in grey.

range-resolution, which allows small-scale scattering features, such as zooplankton thin layers, and individual scatterers, such as fish, to be imaged (Stanton *et al.*, 2010), as well as providing the spectral response of such features. In regions where turbulent microstructure dominates the scattering, improved range resolution can improve the resolution of acoustic inferences of parameters such as dissipation rates of turbulent kinetic energy, which are relatively coarsely determined (typical resolution 0.5–1 m) by direct microstructure instruments.

The high-frequency broadband scattering system has been used to measure scattering from oceanic microstructure and zooplankton in the presence of non-linear internal waves propagating over the New Jersey continental shelf, and results of these measurements are presented here. High-resolution images of many internal wave trains have been obtained at different stages of their evolution. Coincident direct microstructure measurements were performed for all the non-linear internal waves sampled acoustically. A restricted number of zooplankton net tows were also performed to characterize the zooplankton present on the New Jersey continental shelf at the time of the experiment. Here, the EdgeTech broadband system and the modifications needed to perform high-frequency broadband scattering measurements are described, details of the calibration are presented, and the system's performance is evaluated. Emphasis is given to aspects of this system that are new. Evidence is presented that there are regions of the internal waves in which the scattered broadband

spectra are consistent with scattering dominated by zooplankton vs. oceanic microstructure. This has also been observed previously in regions of internal waves (Warren *et al.*, 2003) using four narrowband acoustic frequencies (43, 120, 200, and 420 kHz). Simple inversions of the broadband acoustic data result in zooplankton and microstructure parameters that are consistent with measurements made by a direct microstructure instrument and zooplankton net tows.

System description

The high-frequency broadband scattering system is a custom configured sidescan sonar system developed by EdgeTech. The EdgeTech sidescan sonar system is typically used in a towed configuration with either one or two individual narrowband frequencies (although there are three independent channels available to use). The narrowband frequencies can be user-specified up to a frequency of 600 kHz. To maintain flexibility, the system was designed to be fully programmable and capitalizes on broadband signal-processing techniques. Therefore, only small changes were necessary to both the hardware and the software to accommodate four customer-supplied broadband piston-like transducers [LOW, MID, High–Low (HL), and High–High (HH)], manufactured by Airmar Technology Corporation (35 Meadowbrook Drive, Milford, NH, USA), with mostly overlapping frequencies ranges spanning 150–600 kHz almost continuously (Table 1). Although each transducer had separate hardware for signal generation and detection (including power amplifiers and A/D converters), there are software limitations that impose a maximum of three independent channels. As there are only three fully independent channels, but four almost octave-bandwidth broadband transducers were necessary to span the range 150–600 kHz, channel 3 was shared between the HL and HH transducers, resulting in modifications to the sampling strategy, described in detail below.

Hardware

The EdgeTech electronics are housed in an 8-inch outer diameter by 34-inch long, aluminium, underwater can, depth rated to 1000 m. The EdgeTech electronics are controlled by a Windows XP embedded PC104 card (Pentium 3, 800 MHz). Also included in the EdgeTech underwater unit are an internal hard drive for data storage (80 GB capacity), custom-built Transmit/Receive (T/R) switches and 200 W linear power amplifiers for each broadband transducer, and an integrated motion sensor (pitch, roll, and heading; Figure 2). The transmitted waveforms are pre-generated and stored on the computer in the underwater unit. The digital waveform is converted to an analogue signal via a 10-bit DAC card with an 8 MHz sampling rate. The echoes are digitized in the underwater electronics unit with a 16-bit D/A converter running at 1.2 MHz, limiting the highest frequency to 600 kHz to satisfy the Nyquist sampling criterion. An analogue gain of 0.27 dB m^{-1} (ramp formula provided by EdgeTech) was applied to the data in hardware and corrected for in post-processing.

A deck unit converts AC power to DC power and provides ± 400 V to the underwater unit over a Kevlar-reinforced coax cable 1000 m long and 0.322 inch diameter. Power, communication with the computer in the underwater unit, and digital data are transferred over the coax cable. The underwater computer is powered up when the deck unit is turned on. A laptop computer (running Windows 2000, and from this point on called the deckside computer) was used to control and communicate with the computer in the underwater unit through an ethernet cable connected to the deck unit. The data could be stored either in the underwater unit or telemetered in real time (maximum data transfer rate of $\sim$4.5 Mbits s^{-1}) and saved on the deckside computer. In this latter mode, the data are displayed in real time by the "JStar" software provided by EdgeTech. Both the raw and compressed-pulse data were stored. GPS data, including time, latitude, and longitude, can be integrated into the system through a serial port (RS-232) on the topside computer. A customer-supplied CTD (conductivity, temperature, depth) sensor (Seabird FastCAT model SBE49: titanium housing depth rated to 7000 m, 16 Hz sampling rate, and strain gauge pressure sensor depth rated to 350 m) was interfaced with the EdgeTech underwater unit. Power to the CTD was provided by the EdgeTech underwater unit.

Table 1. Transducer and channel parameters.

Transducer parameters	LOW	MID	HL	HH
Frequency range (kHz)	160–270	220–330	330–470	450–590
Nominal centre frequency (kHz)	200	270	380	500
Nominal transducer radius (mm)	25.5	18.5	10	12
Inferred transducer radius (mm)	23.9	16.2	9.9	12.4
Nominal full beamwidth (°) at centre frequency	8.6	8.8	11.6	7.4
Inferred full beamwidth (°) at centre frequency	9.3	10.2	11.9	7.2
Source level (dB re 1 μPa per 1 m)	188	186	179	192
Band-averaged noise levels (dB)	−85.4	−81.8	−71.1	−74.1

The transducer housings were made of PVC, depth rated to 100 m. The source levels were provided by EdgeTech. Noise levels were averaged across the band.

Profiling platform

Because of considerations of transmission loss at high frequencies and changes in sampling volume with range, the system was designed to be profiled vertically or held at a constant depth, instead of towed. A high-grade stainless-steel frame was designed that included a rotatable plate on which the four broadband transducers were mounted. The transducer mounting plate could be rotated 90° between either a profiling side-looking mode, with the transducers facing horizontally, or a constant-depth mode, with the transducers facing vertically down. The transducer plate was easily aligned into either of these configurations by an alignment pin. A stabilizing fin was added to the frame to minimize rotation during deployment attributable to subsurface currents.

Transmitted signals

The transmitted waveforms and signal gains are programmable and were generated within the software provided by EdgeTech, resulting in either CW signals or linear frequency modulated sweeps (or chirps) with full control of the frequency bandwidth, signal duration, and amplitude. All data collected in this study involved chirps of either 500 μs or 5 ms duration. The optimal signal duration is determined by a balance between improved signal-to-noise ratios (SNRs) for longer transmit signals, and a

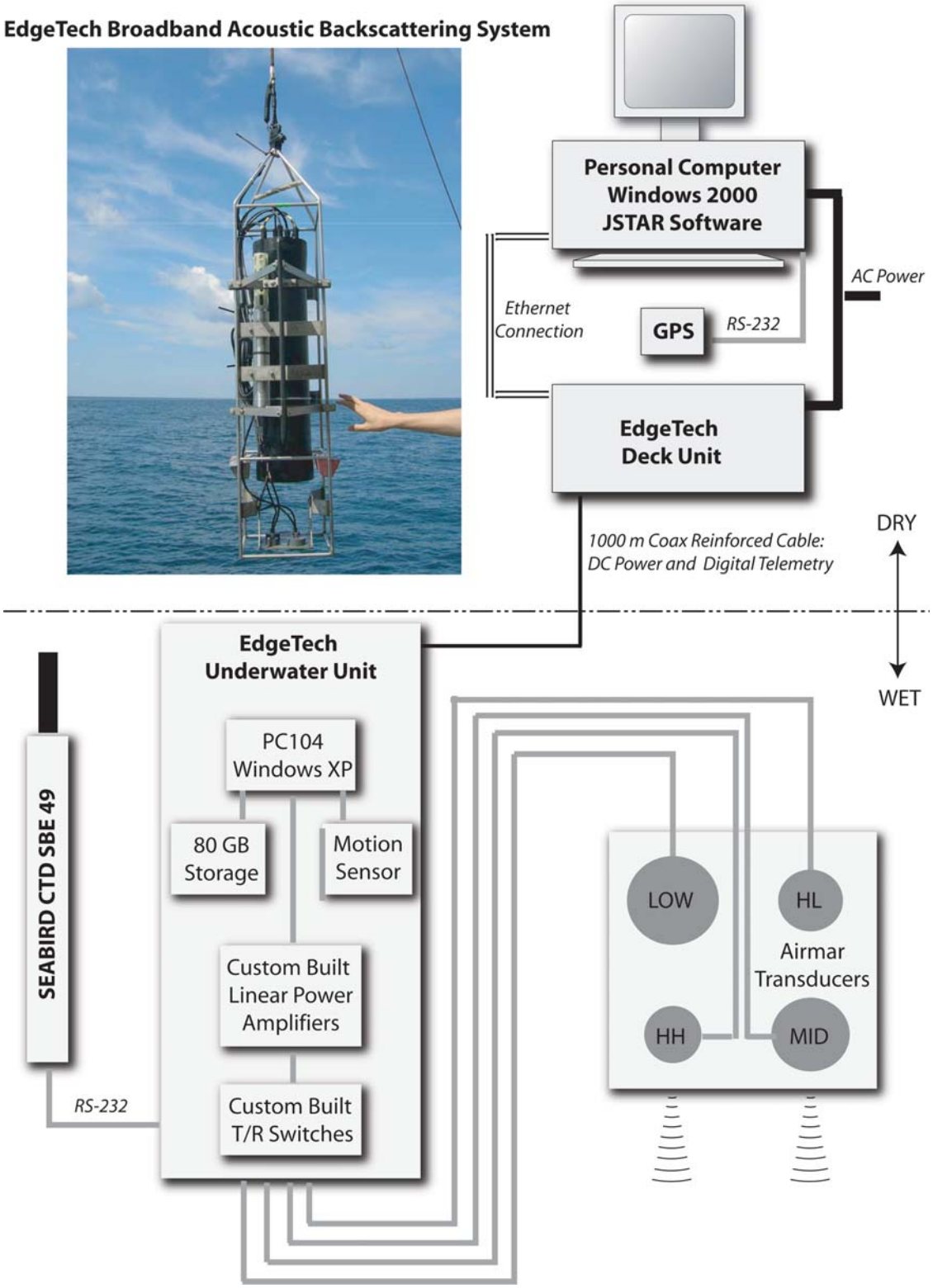

Figure 2. The EdgeTech high-frequency broadband scattering system and a block diagram of the associated electronics.

smaller blanking region at short ranges with shorter transmit signals. The SNR was significantly higher when the 5-ms rather than the 500-μs pulse length was used, but the blanking region increased from ~50 cm to almost 2 m.

The signals for the three independent channels can be transmitted simultaneously or sequentially, with full control over the order and time intervals between channels and the time interval between each transmitted sequence (referred to here as the ping

rate). Owing to the overlapping bandwidths and the fact that the HL and HH transducers shared a channel, the transmit sequence chosen was LOW, MID, HL, LOW, MID, HH, with 333 ms between channel transmissions. The typical ping rate for the entire sequence was therefore 0.5 Hz: the LOW and MID channels sampled the water column once per second, whereas the HL and HH channels only sampled once every 2 s. Data were typically collected to a range of 50 m.

Signal processing

The broadband capabilities of the system are exploited through pulse-compression signal processing techniques (Turin, 1960; Chu and Stanton, 1998; Stanton and Chu, 2008; Stanton *et al.*, 2010), which are based on matched filter processing and involve cross-correlating the echo-voltage time-series, $v_r(t)$, with the transmitted signal voltage time-series, $v_t(t)$ (which is used as the replica signal):

$$\mathrm{cp}_r(t) = k_{\mathrm{cp}} v_r(t) \otimes v_t(t), \quad (1)$$

where $\otimes$ represents cross-correlation, cp_r the compressed-pulse output, and the normalization factor k_{cp} the inverse of the auto-correlation function of $v_t(t)$, evaluated at zero time-lag. This type of processing results in significantly increased temporal (and hence range) resolution and increased SNR (see Discussion in Stanton and Chu, 2008). The duration of the main lobe of cp_r is approximately equal to the inverse bandwidth of the transmitted signal, $1/B$, and the increase in SNR is approximately equal to $2\,BT$, where T is the signal duration.

Methods

Calibration procedure

Various calibration methods for broadband systems have been suggested (Dragonette *et al.*, 1981; Atkins *et al.*, 2008; Stanton and Chu, 2008), and the approach taken here combines some aspects of these techniques. A spherical, 20-mm-diameter, tungsten carbide with 6% cobalt standard target (denoted throughout this manuscript as WC20) was used to calibrate the system. Standard target calibrations rely on the availability of an accurate scattering model for the target, for which the material properties and dimensions are well known (Foote and Maclennan, 1984). The Woods Hole Oceanographic Institution (WHOI) EdgeTech broadband system was calibrated (i) in a controlled laboratory tank before the field deployment, (ii) in a sea-well 14 m deep abutting WHOI both before and after the field experiment, and (iii) *in situ* in water 50 m deep to assess any effects on the calibration attributable to changes in pressure with depth.

Tank calibration

The laboratory calibration was performed on 15 and 16 June 2006. The tank was 1.5 m deep, 2.4 m wide, and 3.6 m long and filled with filtered (5 μm) seawater. The system was lowered to the bottom of the tank and placed on its side, with the transducers facing vertically upwards, and the standard target suspended directly above the transducers at a range of 0.75 m. To centre the sphere in the beam for each transducer, the position of the standard target was adjusted to maximize the amplitude of the compressed-pulse output. Once the target was centred in the beam, the target was moved in small increments parallel to the transducer face to provide a crude map of the beam pattern as a function of frequency that could be compared with the theoretical beam pattern of a piston-like transducer of known dimension. The tank temperature and salinity were measured to determine the sound speed of the seawater in the tank accurately. Because of the restricted range available for the controlled laboratory measurements, the beam patterns were only measured using the 500-μs signals.

Sea-well calibration

The sea-well calibration was performed both before (7 July 2006) and after (30 August 2006) the field experiment, for both 5 ms and 500 μs signals. The system was suspended in vertical mode with the standard target directly below the transducers at ranges between 3.9 and 5.25 m. System pitch-and-roll measurements were made and used to eliminate echoes for which the system was not aimed vertically. Temperature and salinity were recorded to determine the sound speed of the surrounding water.

In situ *calibration*

The *in situ* calibration was performed on 13 August 2006, also with the system in vertical mode and the standard target suspended directly below the transducers at a range of 2.2 m. This calibration was only performed for the 500-μs signal at two depths (5.25 and 20.3 m) because the increasing pressure with depth can affect the sensitivity of the transducers. Temperature and salinity were recorded as a function of depth to allow the sound-speed profile to be inferred accurately. The measured scattering was greater at 20.3 m than at 5.25 m for the LOW and HH channels, by 0.3 and 0.9 dB, respectively, and smaller at 20.3 m than at 5.25 m for the MID and HL channels, by 2.2 and 1.5 dB, respectively. Most of the data presented here were collected with the broadband system suspended close to the surface (~5 m deep).

General

All data, from the calibrations and the field experiments, were collected with the system operating at 100% power output, except for the LOW and MID frequency channels during the laboratory tank calibration. Owing to the restricted range in the laboratory tank, the returns from the standard target were saturated when full power was employed because of the limited dynamic range of the system. Instead, the LOW and MID frequency channels were operated at ~0.5 and 2.25% power (corresponding to 7 and 15% of the maximum amplitude output). In addition, during the *in situ* calibration, the LOW channel was operated at 25% power to prevent saturation because the standard target was at a range of just 2.2 m. The linearity of the compressed-pulse output with increasing power (above ~0.5%) was verified.

As a final note, the frequency response of the system can be determined theoretically by looking at normal incidence scattering from the air–water interface, so long as the surface roughness is small compared with the wavelength. Even at the relatively high frequencies of this work, this assumption is valid in the laboratory tank environment. However, although this method of calibration was attempted, the returned signal was saturated at all levels of power output that were in the linear regime. This calibration was also attempted in a tank 6 m deep, but the air–water interface returns were still saturated.

Calibration curves

The measured frequency spectrum of the WC20 calibration sphere was in relatively good agreement with the theoretical target strength (*TS*) across the frequency bands of interest (Figure 3a),

from which it was possible to determine the calibration curves (defined in the following section) needed to perform a system calibration (Figure 3b). Errors in the calibration curves at frequencies close to the resonance frequencies can be quite large. To minimize this, a cubic spline fit was used close to these frequencies. The approach assumes that the transducer response does not vary significantly over this frequency range, an assumption confirmed later by a calibration study with two standard targets of different size. Finally, there is a clear ± 2.5 dB discrepancy between the measured and the predicted WC20 *TS* for the HH channel, for which the general trend was an increasing underprediction of the theoretical *TS* with increasing frequency. This discrepancy may be due to the standard target not being close to the centre of the transducer beam pattern, although this discrepancy was observed in all calibrations. Because of these discrepancies, which result in calibration-dependent structure in the spectra measured in the field, the mean value across the band was used instead of the frequency-dependent calibration curve for the HH channel.

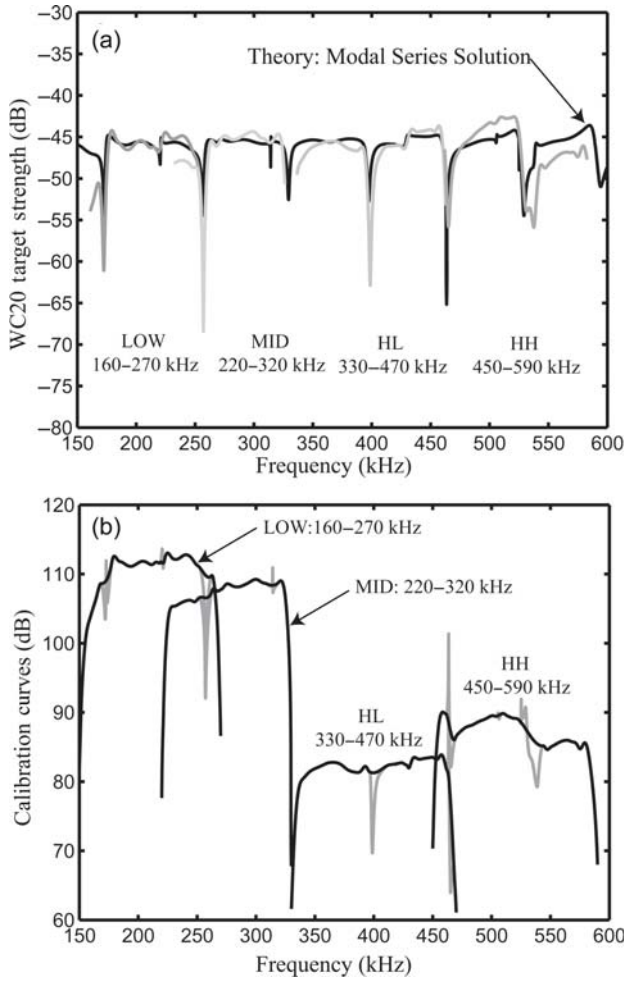

Figure 3. (a) Comparison of the predicted and measured frequency response of a 20-mm-diameter tungsten carbide with 6% cobalt standard target (WC20). The measured curves have been shifted uniformly and arbitrarily to give the best agreement with the predicted *TS*. The difference between the predicted and measured WC20 response corresponds to the calibration curves. (b) Calibration curves (grey) as a function of frequency for the LOW, MID, HL, and HH frequency channels. A cubic spline fit (black) was used close to the resonance frequencies to obtain the usable calibration curves.

Beam pattern

Knowledge of the transducer beam pattern is necessary to convert the compressed-pulse output to volume-backscattering strength. The beam pattern of each transducer was crudely measured in the tank by moving the WC20 standard target through small increments along the main transducer axis. For each transducer, a least-squares fit of the measured beam pattern to the two-way predicted beam pattern for an ideal piston transducer was performed at frequency increments of 1 kHz, allowing the equivalent transducer radii to be determined (Table 1). For all transducers except the MID frequency transducer, the inferred and nominal radii were in good agreement, resulting in differences corresponding to <0.6 dB. For the MID frequency channel, the inferred and nominal transducer radii resulted in differences ~ 1 dB (Figure 4).

Conversion of compressed pulse output to volume-backscattering strength

From the compressed-pulse output, the volume-backscattering coefficient as a function of frequency for multiple unresolved targets or for a distributed scattering source in the beam is evaluated as follows [modified form of Equation (11) of Stanton *et al.*, 2010]:

$$s_v(\omega) = \frac{\langle |\mathrm{CP}_r^{\mathrm{vol}}(\omega)|^2 \rangle}{\langle |\mathrm{CP}_{r\_0}^{\mathrm{cal}}(\omega)|^2 \rangle} \quad \left| \frac{L^{\mathrm{cal}}(\omega)}{L^{\mathrm{vol}}(\omega)} \right|^2 \quad \frac{\sigma_{\mathrm{bs}}^{\mathrm{WC20}}(\omega)}{V(\omega)}, \qquad (2)$$

where ω is the angular acoustic frequency, $|\mathrm{CP}_r^{\mathrm{vol}}(\omega)|$ the absolute value of the Fourier transform of the compressed-pulse output from the volume of interest, $|\mathrm{CP}_{r\_0}^{\mathrm{cal}}(\omega)|$ the absolute

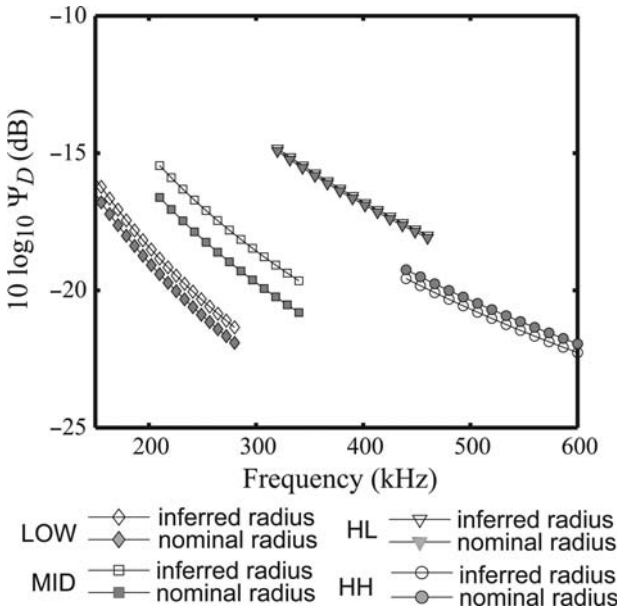

Figure 4. Logarithmic form of the equivalent beam angle, $10 \log_{10} \Psi_D(\omega)$, as a function of frequency for the LOW (diamonds), MID (squares), HL (inverted triangles), and HH (circles) channels. The open symbols correspond to transducer radii inferred from laboratory beam-width measurements, and the solid symbols to nominal transducer radii supplied by the manufacturer.

value of the Fourier transform of the compressed-pulse output obtain during the WC20 standard target calibration, and averages, denoted by $\langle \ldots \rangle$, are taken over a number of pings. $\sigma_{\mathrm{bs}}^{\mathrm{WC20}}(\omega)$ is the theoretically predicted backscattering cross section (based on the exact modal series solution) of the WC20 standard target, which is equivalent to the square of the magnitude of the predicted backscattering amplitude, $F_{\mathrm{bs}}^{\mathrm{WC20}}(\omega)$. The *TS* for the WC20 standard target is given by $TS^{\mathrm{WC20}}(\omega) = 10\log_{10}\sigma_{\mathrm{bs}}^{\mathrm{WC20}}(\omega) = 10\log_{10}|F_{\mathrm{bs}}^{\mathrm{WC20}}(\omega)|^2$, which is illustrated in Figure 3. The combination of terms $10\log_{10}\langle|\mathrm{CP}_{r\_0}^{\mathrm{cal}}(\omega)|^2\rangle - 10\log_{10}\sigma_{\mathrm{bs}}^{\mathrm{WC20}}(\omega)$ is evaluated for each of the channels independently and results in the calibration curves (Figure 3b). $V(\omega)$ is the frequency-dependent equivalent insonified volume at range r_{vol} and is given by

$$V(\omega) = \frac{1}{2}cTr_{\mathrm{vol}}^2\Psi_D(\omega) = Lr_{vol}^2\Psi_D(\omega), \tag{3}$$

where c is the speed of sound in water, T the duration of the time-window (after the pulse-compression processing) encompassing the volume of interest, such that the "size" of the volume is $L = cT/2$, and the equivalent beam angle Ψ_D (ω) is defined in Urick (1983). $L^{\mathrm{vol}}(\omega)$ and $L^{\mathrm{cal}}(\omega)$ represent the transmission loss on a linear scale for the calibration and scattered signals attributable to spherical spreading and seawater absorption. The absolute value of the ratio of these terms is given by

$$\left|\frac{L^{\mathrm{cal}}(\omega)}{L^{\mathrm{vol}}(\omega)}\right| = \frac{r_{\mathrm{vol}}^2}{r_{\mathrm{cal}}^2}10^{2\alpha(\omega)(r_{\mathrm{vol}}-r_{\mathrm{cal}})/20}, \tag{4}$$

where r_{cal} is the range from the transducer to the WC20 standard target during the calibration measurement, and α is the frequency-dependent attenuation factor (in dB m^{-1}) attributable to absorption (Figure 7 of Francois and Garrison, 1982), and is a function of temperature and salinity.

The volume backscattering strength $S_v = 10\log_{10}s_v$, with units of decibels relative to 1 μPa at 1 m, is the logarithmic equivalent of Equation (2). S_v as a function of frequency is referred to as a scattering spectrum throughout this work.

Display of calibrated compressed-pulse data

Display of the calibrated compressed-pulse data from all channels on the same scale as a function of range and ping number (or time), so that it is a representation of volume scattering (in much the same way that a narrowband system might display calibrated echograms at separate frequencies as a function of time and depth), is not intuitive. The compressed-pulse data contain contributions from all frequency components of the signal, the sampling volume is changing as a function of range and frequency, and each channel has a different frequency-dependent calibration. These factors need to be compensated for to display the compressed-pulse data from the different channels on a similar scale to resemble traditional echograms. The compressed-pulse data in a given channel are displayed on a logarithmic scale as follows:

$$10\log_{10}\left(\left|\frac{cp_r(t)}{cp_{r\_0}^{\mathrm{cal}}(t_c)}\right|^2\left|\frac{L^{\mathrm{cal}}(\omega_c)}{L^{\mathrm{vol}}(\omega_c)}\right|^2\frac{\sigma_{\mathrm{bs}}^{\mathrm{WC20}}(\omega_c)}{r_{\mathrm{vol}}^2\Psi_D(\omega_c)}\right), \tag{5}$$

where ω_c is the centre frequency of the channel, and t_c is the time delay that corresponds to the maximum in the compressed pulse arrival of the standard target. Although this does not accurately account for the frequency dependence of the various factors, the compressed-pulse output with the scaling given by the expression in Equation (5) is adequate for illustration purposes, although it is not used for analysis.

Field application

The high-frequency broadband scattering system was used to measure scattering from oceanic microstructure and zooplankton during the generation, propagation, and dissipation of non-linear internal waves over the New Jersey continental shelf from 29 July 2006 to 27 August 2006 on board the RV "Oceanus". Surface-trapped non-linear internal waves of depression result in advantageous signals for shipboard testing of this system. They are both intensely turbulent (Moum *et al.*, 2003) and shallow, resulting in high signal levels within the relatively short range of surface-deployed high-frequency broadband acoustics. The measurements were part of the Navy-funded Shallow Water 2006 Acoustics and Non-Linear Internal Waves Experiments (Tang *et al.*, 2007).

The broadband acoustic system collected data while a direct microstructure instrument, Chameleon (Moum *et al.*, 1995), developed at Oregon State University, was profiled simultaneously. Both systems were deployed with the vessel slowly drifting, and the internal waves were sampled as they passed the vessel. Once the internal wave passed, the instruments were recovered, the vessel rapidly moved ahead of the internal wave and the instruments were redeployed. Thus, the same internal wave train was sampled on multiple occasions as it propagated across the continental shelf.

Zooplankton net tows

Four oblique zooplankton net tows were performed with a 1-m^2 Multiple Opening/Closing Net and Environmental Sampling System (MOCNESS; Wiebe *et al.*, 1985) to characterize the zooplankton present during the experiment and to determine the contribution to scattering from zooplankton in the study area (Table 2). It was not possible to deploy both the MOCNESS and broadband scattering system simultaneously. The MOCNESS had ten 200-μm nets, the first net (net 0) sampled from the surface down to a few metres above the seabed, and the subsequent nine nets (although sometimes fewer were used depending on water depth) sampled quantitatively in small depth bins ($\sim$7–12 m net^{-1}) from close to the seabed to the surface. The procedures followed for sample preservation and analysis are detailed in Lavery *et al.* (2007), who also discuss the well-documented problems of net avoidance, escapement, and destruction of fragile animals by nets.

The four MOCNESS tows (labelled 2–5) performed on the New Jersey continental shelf were fully analysed for zooplankton composition, size, and abundance. Detailed results for tow 4, performed on 24 August 2006, and tow 5, performed on 26 August 2006, are presented here (Figure 5). The two internal waves discussed in this study, imaged on 14 and 22 August, 2006, were at a distance of 20.0 and 12.6 km from tow 4, and a distance of 11.0 and 5.6 km from tow 5, respectively. Although tows 2 and 3, performed on 10 and 13 August 2006, respectively, were temporally closer to the first internal wave, they were significantly more distant and the water depth was shallower (40 m). As a result of the relatively large spatial and temporal separation between the net tows and the acoustic measurements, the

Table 2. Time and locations of MOCNESS zooplankton net tows and the two internal waves discussed in this study.

Type	Date	Time (GMT)	Full water-column depth (m)	Latitude (N)	Longitude (W)
MOC 2	10 August 2006	19:39	44	39°11.7010′	73°22.8760′
MOC 3	13 August 2006	17:34	40	39°19.4864′	73°38.9154′
MOC 4	24 August 2006	14:34	64	39°05.3810′	73°16.1320′
MOC 5	26 August 2006	14:48	70	39°04.6340′	73°09.3717′
Internal wave 1	14 August 2006	04:20	75	39°00.8370′	73°03.4780′
Internal wave 2	22 August 2006	08:00	70	39°01.6500′	73°08.8520′

The times and locations for the internal waves indicate the start of the first internal wave trough.

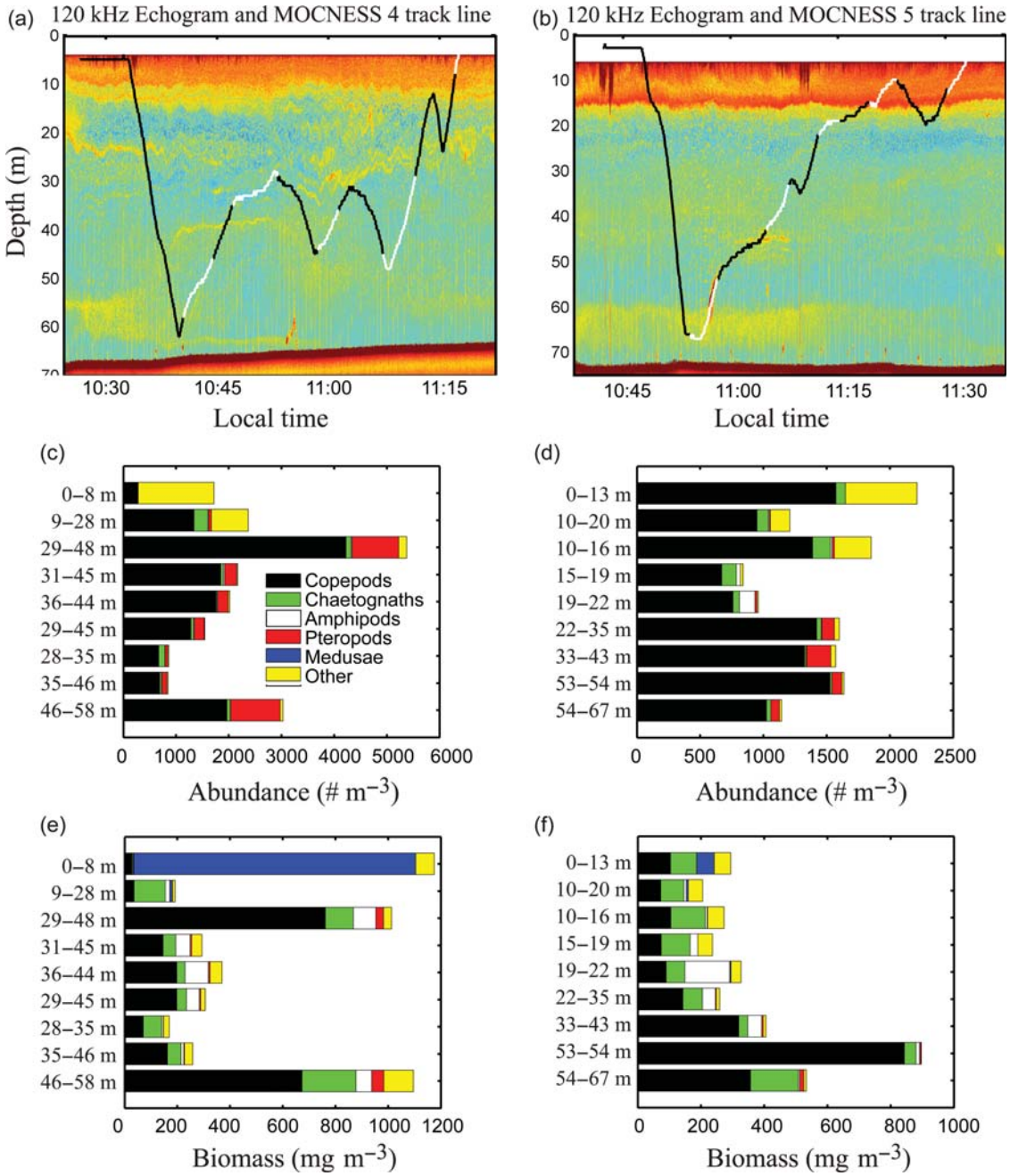

Figure 5. Results of zooplankton net tows for MOCNESS 4 (24 August 2006, left column) and MOCNESS 5 (26 August 2006, right column). (a and b) Track line superimposed on the traditional, narrowband, uncalibrated, hull-mounted 120-kHz echogram. The alternating black and white lines indicate the depths of each net. (c and d) Numerical abundance (m^{-3}) of zooplankton in the different nets. (e and f) Biomass (mg m^{-3}) of zooplankton in the different nets.

biological ground-truthing information obtained from the nets can only be used as a rough guide for interpreting the acoustic measurements.

Zooplankton abundance and biomass were dominated by weakly scattering fluid-like copepods, with larger copepods (mean length 1.5 mm) close to the seabed and smaller copepods (mean length 0.8 mm) close to the surface. Mean copepod lengths in all nets for MOCNESS 4 and MOCNESS 5 were 1.16 and 1.2 mm, respectively. However, predictions of acoustic scattering based on the zooplankton size and abundance in each net (Figure 6), and on models described in Lavery *et al.* (2007), show that the scattering was often dominated by small elastic-shelled pteropods (mean diameter 0.4 mm with observed abundances of up to 1000 per m^3), and amphipods, weakly-scattering fluid-like zooplankton that were generally larger (mean length 4.1 mm) than the copepods observed. Mean pteropod diameters were 0.38 and 0.46 mm, respectively. The abundance of gas-bearing siphonophores was very low, and their contribution to predicting scattering was correspondingly small. No fish larvae were found in the net tows, although they would be expected to avoid such sampling gear, as would most myctophids. The total predicted scattering from all zooplankton in each net is shown in Figure 1, from which it can be seen that for all nets, the total predicted scattering increased with frequency across the available frequency, except for one net that was generally flat across the frequency band (MOC 4 net 5).

High-resolution acoustic images of non-linear internal waves

Using pulse-compression signal processing, high-resolution broadband acoustic images of multiple internal wave trains were obtained at different stages of their evolution (Figure 7). The water column was strongly stratified throughout the entire experiment, with the seasonal thermocline at ~15–20 m. The passage of the non-linear internal waves displaced these isotherms downwards, by as much as 20 m. Strong scattering at and above the depth of the thermocline was often observed, particularly at night, and it was modulated by the passage of the internal waves. On many occasions the scattering from that layer was stronger at the bottom of the internal wave cycles, potentially because of the enhanced shear near the wave troughs creating small-scale shear instabilities that break and cause enhanced turbulence (Moum *et al.*, 2003). At many locations, additional scattering layers were observed, typically deeper than the seasonal thermocline. There were many occasions on which the typical signatures associated with the development and progression of Kelvin–Helmholtz shear instabilities (Smyth *et al.*, 2001; Moum *et al.*, 2003) were observed (Figure 7). Echoes with scattering characteristics consistent with scattering from larger individual marine organisms (e.g. shrimp, fish, fish larvae, myctophids, or squid) were also occasionally observed.

The broadband scattering images have significantly higher resolution in both the vertical and horizontal direction compared with some directly measured microstructure parameters, such as the dissipation rate of turbulent kinetic energy (Figure 8). This is a result of the slow profiling rate for the direct microstructure profiler, typically one profile every 2–3 min, depending on water depth, compared with a ping rate of 0.5–1 Hz, and also because it is necessary to use significant depth bins (0.5–1 m) to obtain adequate estimates of dissipation rate of turbulent kinetic energy (Moum *et al.*, 1995). In contrast, the vertical resolution for the broadband acoustic system is set by the inverse bandwidth, which corresponds to a couple of centimetres.

Measured broadband spectra

The analysis presented here focuses on two contrasting non-linear internal waves. The first, imaged on 14 August 2006, highlights an internal wave (Figure 7a and b) for which there is physical

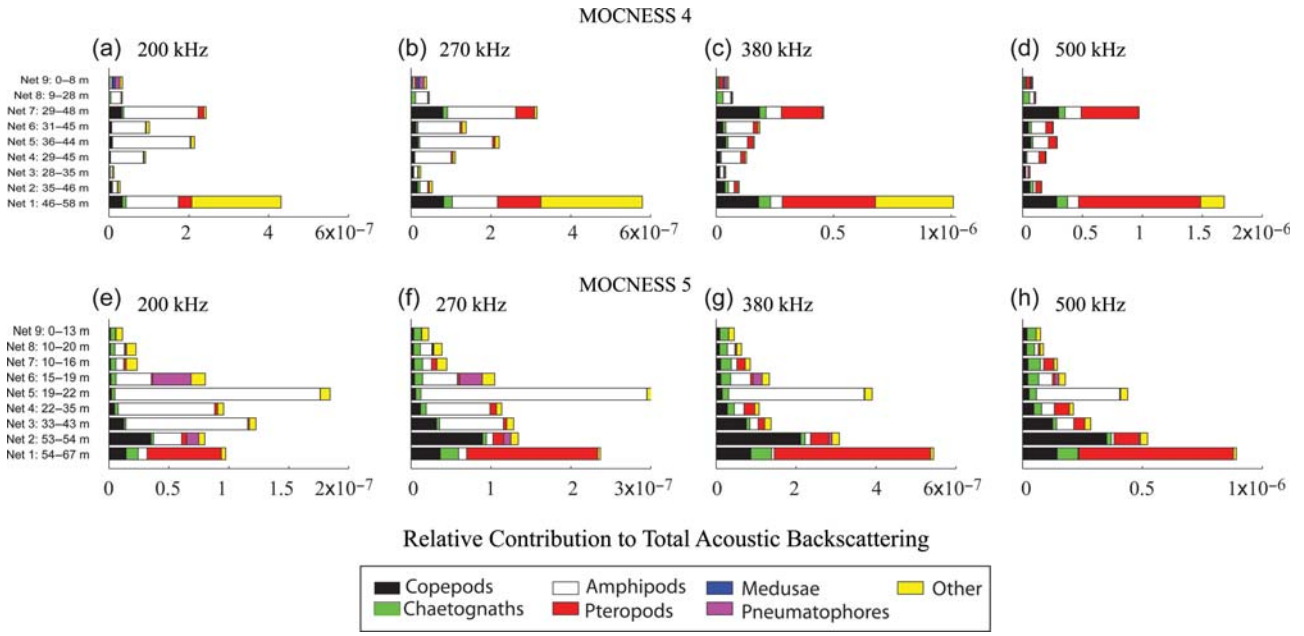

Figure 6. Relative predicted contribution to total scattering from different zooplankton collected in (a–d) the MOCNESS 4 (24 August 2006), and (e–h) the MOCNESS 5 (26 August 2006) at the centre frequencies of the four channels.

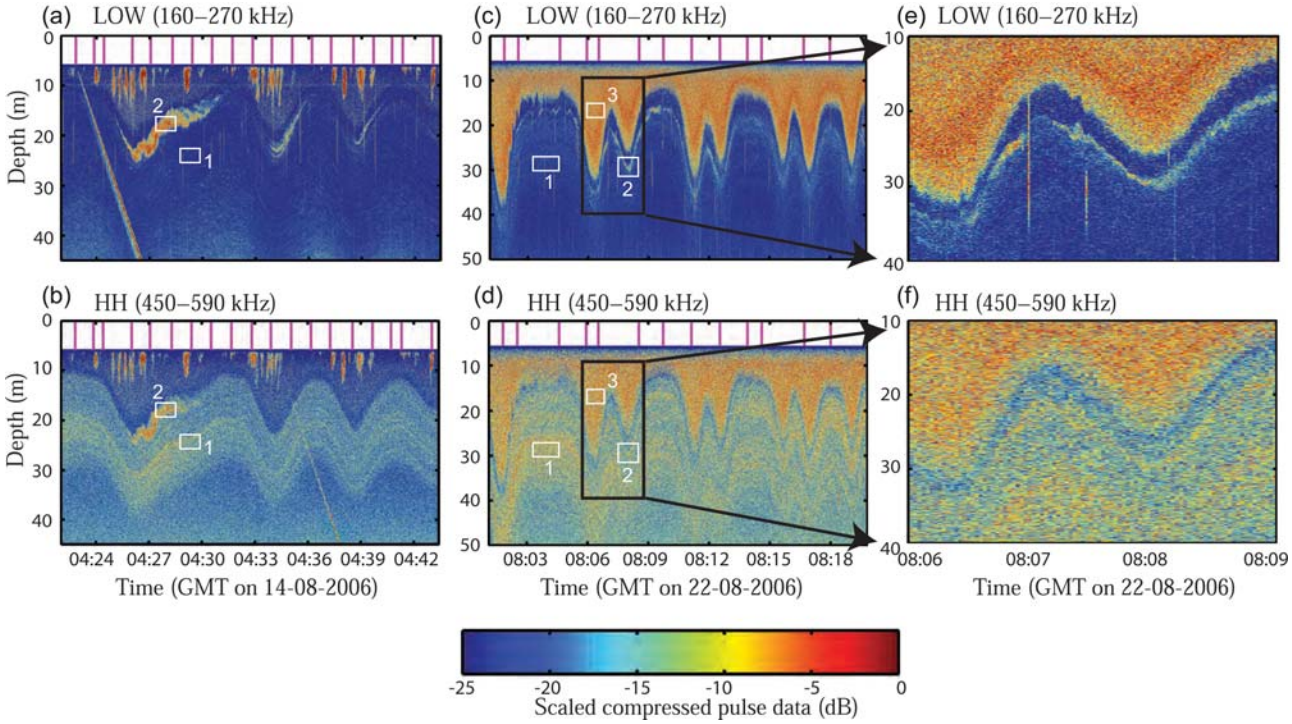

Figure 7. Amplitude of the calibrated compressed-pulse output [Equation (5)] vs. time: (a) LOW and (b) HH frequency channels for the internal wave imaged on 14 August 2006. (c) LOW and (d) HH frequency channels for the internal wave imaged on 22 August 2006. A close up look of the region in the black box in (c) and (d) is shown in (e) and (f), respectively. The white numbered boxes mark the regions that have been used to calculate the spectra shown in Figures 9 and 10. The vertical lines at the top of (a)–(d) indicate the times of the direct microstructure profiles.

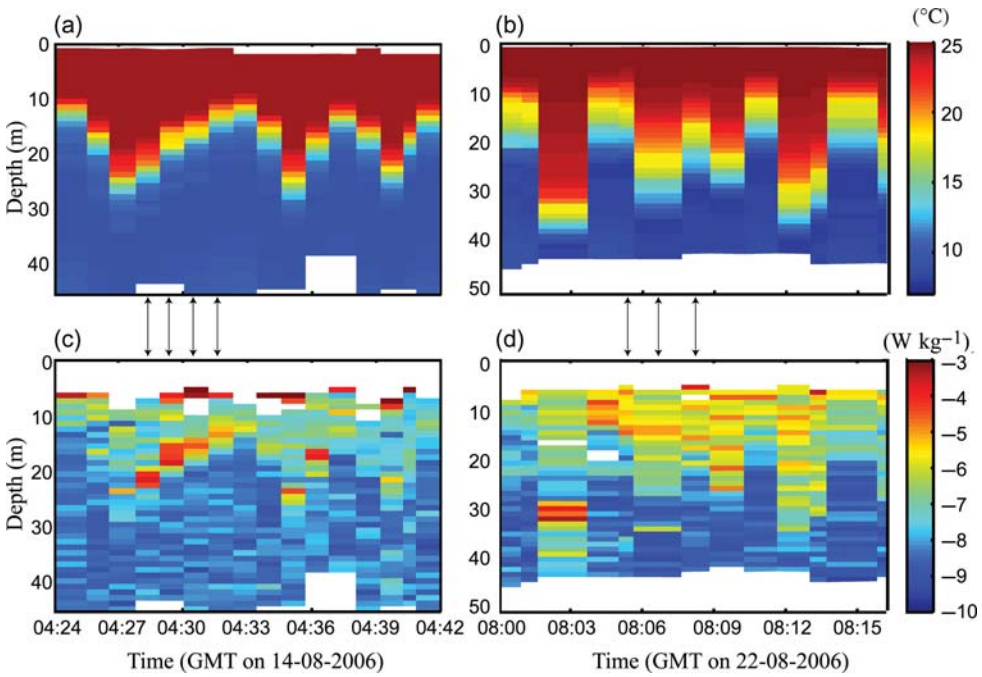

Figure 8. (a and b) Temperature (°C) and (c and d) dissipation rate of turbulent kinetic energy, ε (W kg^{-1}), on a log scale, as measured by the direct microstructure profiler on 14 and 22 August 2006. The measurements were collected at the same time as the broadband acoustic data illustrated in Figure 7. The arrows indicate the profiles plotted in Figure 11 for comparison with the acoustic inferences of ε.

separation between two scattering features and for which the scattering spectra (Figure 9) are distinct, and consistent, across the entire frequency band, with scattering dominated by zooplankton vs. microstructure. The second example, imaged on 22 August 2006, highlights an internal wave (Figure 7c–f) for which the scattering for one particular feature is consistent with a mixture of scattering from zooplankton and microstructure (Figure 10). This second example more clearly highlights the benefits of broadband acoustics, although the first example more persuasively illustrates scattering from turbulent microstructure.

Non-linear internal wave imaged on 14 august 2006: distinct spectra

The first wave (Figure 7a and b) exhibited (i) a diffuse scattering layer below the seasonal thermocline that was most clearly observed on the higher frequency channels, and (ii) a series of Kelvin–Helmholtz shear instabilities, associated with the high dissipation rates measured by the direct microstructure profiler (Figure 8), and that was most clearly observed on the lower-frequency channels. As observed previously (Moum *et al.*, 2003), the scattering from the Kelvin–Helmholtz instability associated with the first cycle of the non-linear internal wave is typically the strongest, and this feature is the focus of the analysis below.

The scattered spectra associated with these two features followed different trends (Figure 9). The scattering from the deeper, more diffuse scattering layer (region 1 in Figure 7a and b) increased rapidly with increasing frequency, increasing by almost 20 dB over the frequency range investigated. In contrast, the acoustic spectrum associated with the Kelvin–Helmholtz shear instability (region 2 in Figure 7a and b) decreased by $\sim$8 dB over the frequency band available. During this experiment, $>$25 non-linear internal waves were tracked over the period of almost a month, and many such Kelvin–Helmholtz shear instabilities were observed acoustically. Spectra that were generally decreasing (by more than a standard deviation of the spectrum noise) across the entire frequency band were almost uniquely associated with shear instabilities.

Non-linear internal wave imaged on 22 august 2006: mixed spectrum

The non-linear internal solitary wave imaged on 22 August 2006 (Figure 7c–f) exhibited (i) a diffuse scattering layer below the seasonal thermocline that was most clearly observed on the higher frequency channels, (ii) a thin scattering layer, spanning $\sim$1 m and located a few metres below the seasonal thermocline, and (iii) strong scattering at and above the seasonal thermocline.

The scattered spectra associated with these features also followed different trends (Figure 10). The scattering from the deeper, more diffuse scattering layer (region 1 in Figure 7c and d) increased rapidly with increasing frequency, increasing by almost 20 dB over the frequency range investigated. This scattering layer was only faintly visible on the 120 kHz single narrowband-frequency hull-mounted echosounder and the LOW broadband channel. The spectrum of scattering from the thin layer located a few metres below the seasonal thermocline (region 2 in Figure 7c and d) initially decreased with increased frequency for the LOW and MID channels (160–330 kHz), then increased with frequency at frequencies corresponding to the HL and HH channels (330–590 kHz). The scattering associated with the layer at and above the thermocline (region 3 in Figure 7c and d) very slowly decreased (typically less than a standard deviation of the spectral noise) across the entire frequency band.

Interpretation of measured broadband spectra

In this section, possible sources for the measured broadband spectra are discussed in the context of the available ground-truthing information. The direct microstructure and

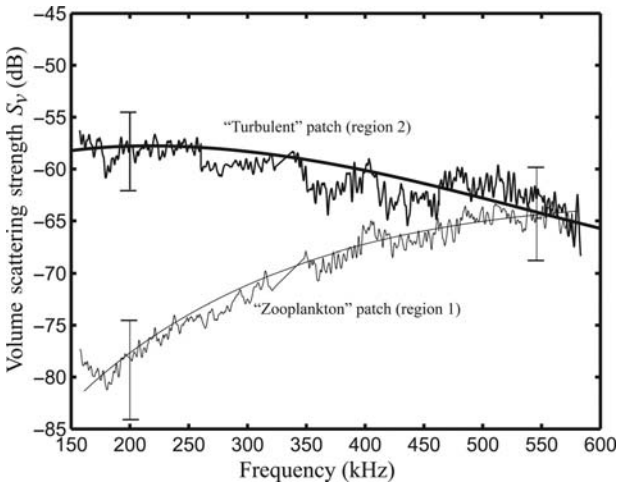

Figure 9. Measured scattering spectra of the regions labelled 1 and 2 in Figure 7a and b during the passage of a non-linear internal wave imaged on 14 August 2006. The thin solid grey line represents the predicted scattering from elastic-shelled pteropods based on inferred size and abundance from least-squares inversions ($r^2 = 0.78$, $p < 0.01$). The thick solid black line represents the predicted scattering from turbulent microstructure based on inferred values of the dissipation rate of turbulent kinetic energy, ε (W kg^{-1}), and temperature variance, χ_T (m^2 s^{-1}; $r^2 = 0.98$, $p < 0.01$). Typical error bars are shown.

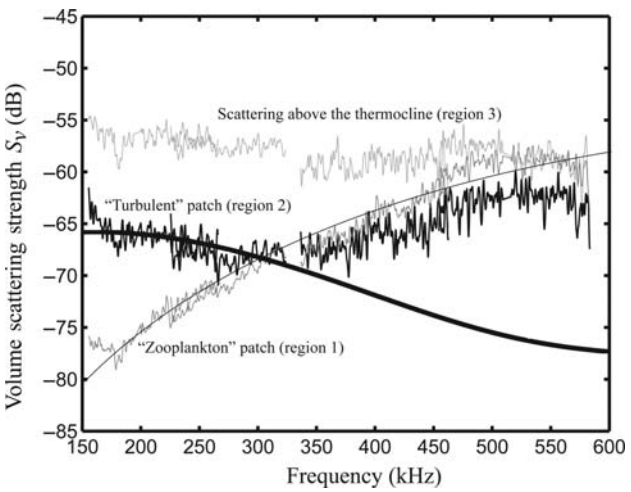

Figure 10. Measured scattering spectra of the regions labelled 1–3 in Figure 7c and d during the passage of a non-linear internal wave on 22 August 2006. The thin solid grey line represents the predicted scattering from elastic-shelled pteropods based on inferred size and abundance from least-squares inversions ($r^2 = 0.98$, $p < 0.01$). The thick solid black line represents the predicted scattering from turbulent microstructure based on inferred values of the dissipation rate of turbulent kinetic energy, ε (W kg^{-1}) and temperature variance, χ_T (m^2 s^{-1}; $r^2 = 0.68$, $p < 0.01$).

broadband acoustic measurements were performed simultaneously (not completely coincidently, because they were separated by a few tens of metres), but the zooplankton net samples were restricted in number and not coincident in space or time with the broadband acoustic measurements, so limiting the certainty of the conclusions, though all the conclusions drawn here are consistent with the results of the direct sampling.

Spectra consistent with scattering from small zooplankton alone

The scattered spectra for the deeper more-diffuse scattering layers (regions 1 in Figure 7) are consistent with Rayleigh scattering of a biological origin, i.e. the spectra rapidly increase with increasing frequency. These scattering features are most likely attributable to small non-gas-bearing zooplankton (e.g. abundant weakly scattering fluid-like copepods or less abundant but more strongly scattering elastic-shelled pteropods), because it appears that the scattering has not yet reached the Rayleigh-to-geometric scattering transition, which, for larger zooplankton such as euphausiids, is at lower frequencies (Table 3). Scattering from organisms with gas inclusions (e.g. gas-bearing siphonophores or fish larvae) is expected to be relatively independent of frequency (ignoring sharp high-order resonances), or even decreasing, in this frequency band. Gas inclusions would have to have radii between 5 and 25 μm to have resonance frequencies in the frequency band available, yet the siphonophore gas inclusions measured in this study, as well as in other studies, are typically larger (Benfield *et al.*, 2003; Lavery *et al.*, 2007).

Spectra consistent with scattering from turbulent microstructure alone

The scattered spectrum for the Kelvin–Helmholtz shear instability imaged on 14 August 2006 (region 2 in Figure 7a and b) is consistent with scattering from temperature microstructure generated by turbulence, i.e. the spectrum decreases with increasing frequency across the available frequency band. Predictions of scattering from turbulent microstructure (using the scattering model described in Lavery *et al.*, 2007) that make use of the coincident direct microstructure measurements indicate that the scattering is typically dominated by temperature microstructure and that the diffusive roll-off in the spectrum for scattering from turbulent temperature microstructure often occurs within the available frequency range. However, salinity microstructure also played an important role at the higher frequencies, and omission of this contribution resulted in poorer quantitative interpretation of the data (discussed in more detail below). It should also be noted that a distribution of microbubbles can be derived that could give rise to a spectrum that decreases across the frequency range 150–600 kHz. Although there are many physical and biological sources of microbubbles (Medwin, 1977), there is no clear generation mechanism that could restrict the presence of such microbubbles almost exclusively to Kelvin–Helmholtz instabilities.

Table 3. Range of organism lengths, L (mm), such that the Rayleigh-to-geometric scattering transition ($ka = 1$, where k is the acoustic wave number and a a typical dimension, such as mean organism radius), is in the frequency band 150–600 kHz.

Parameter	Copepods	Pteropods	Amphipods	Euphausiids
L (mm)	2.03–8.12	0.80–3.18	2.39–9.55	6.59–26.37
L/a	5.1	2.0	6.0	16.57

The length-to-radius values, L/a, are taken from Lavery *et al.* (2007).

Spectra consistent with scattering from a combination of small zooplankton and microstructure

The spectrum of scattering from the thin scattering layer located a few metres below the seasonal thermocline for the internal wave imaged on 22 August 2006 (region 2 in Figure 7c and d, close-up in Figure 7e and f) is consistent with predictions of scattering from turbulent temperature microstructure for frequencies below 330 kHz (the LOW and MID frequency channels). Above 330 kHz, the spectrum of scattering from this layer is consistent with scattering dominated by small zooplankton, for which the Rayleigh-to-geometric scattering transition has not yet occurred. However, this spectrum could also be consistent with scattering from a small number of larger zooplankton, such as euphausiids (Stanton *et al.*, 1998a).

Spectra of unknown origin

Based on the available information, it is difficult to determine conclusively the origin of the scattering at and above the seasonal thermocline (region 3 in Figure 7c and d). The spectrum of scattering is not consistent with either small zooplankton or turbulent microstructure alone. The strong scattering at and above the seasonal thermocline was not observed during daylight as prevalently as it was at night, suggesting that a significant portion of the scattering is attributable to zooplankton that perform daily vertical migration. However, all the zooplankton tows were performed during daylight, so the origin of the scattering observed can only be speculated upon. If the scattering is of biological origin, it must either be larger zooplankton for which the Rayleigh-to-geometric scattering transition has already taken place or be attributable to gas-bearing organisms for which the resonance frequency is <150 kHz, although there was little evidence of gas-bearing zooplankton (or fish, though the zooplankton net-sampling techniques used suffer from significant avoidance from larger nekton) in the daylight zooplankton tows. It is also likely that turbulent microstructure contributes to this scattering layer during the passage of non-linear internal waves. However, particularly at night, this contribution appears to be small compared with the contribution to scattering of a biological origin. Finally, microbubbles with resonance frequencies <150 kHz could also be contributing to the scattering in the upper mixed layer.

Inferences of zooplankton parameters from measured broadband spectra

Least-squares inversions of the broadband scattering data from the deeper diffuse scattering layers (regions 1 in Figure 7) were performed to determine the size and abundance of copepods or pteropods that might be giving rise to this scattering layer. The scattering models and parameters used to make the predictions are described in Lavery *et al.* (2007). These inversions assume single-sized organisms and vary the size and abundance to reduce the least-squares error between the predicted and measured scattering. This was done independently for copepods and pteropods. Although this approach most likely oversimplifies the interpretation of the spectra observed, an inversion that included a mix of zooplankton would have more free parameters to fit. Given the already speculative nature of the interpretation as a result of insufficient biological ground-truthing, this more complex approach was not pursued.

The results of these inversions indicate that for the internal wave imaged on 14 August 2006, the scattering layer could be made up of

$\sim$61 pteropods m^{-3} of diameter 0.78 mm (Figure 9), whereas for the internal wave imaged on 22 August 2006, the scattering layer could be made up of $\sim$960 pteropods m^{-3} of diameter 0.53 mm (Figure 10). In other words, the acoustically inferred pteropod sizes and abundances were in reasonable agreement with the sizes found in the MOCNESS tows.

Although the acoustically inferred size of copepods compared favourably with the sizes measured in the MOCNESS tows, the abundances were not in good agreement. The acoustically inferred abundances were significantly higher, although greater abundance than that observed in the current MOCNESS tows has been documented in the literature (Wiebe *et al*., 1973; Wishner *et al*., 1995), and it is generally recognized that issues such as avoidance and damage to fragile individuals tend to cause net-sampling systems such as the MOCNESS to underestimate the real abundance of many zooplankton organisms. Combining these uncertainties with the patchiness inherent in zooplankton distributions, the limited ground-truthing, and the potentially oversimplified inversion approach, it is not surprising that the inferred copepod abundances were not in good agreement with the MOCNESS data. More surprising is the relatively good agreement in the inferred and directly measured size of copepods and pteropods. In fact, the deeper scattering layer is most likely a combination of pteropods and copepods (and potentially other small zooplankton).

Inversion of broadband acoustic data for the location of the Rayleigh-to-geometric scattering transition (or of a resonance frequency) provides a relatively accurate method for determining size. In contrast, absolute scattering levels are subject to the vagaries of calibration, in addition to which there is uncertainty in the abundance measured by net tows attributable to issues such as avoidance. In the cases presented here, the Rayleigh-to-geometric scattering transition has not yet taken place (Table 3), so the inversion for size is not as robust as it would have been if this transition was in the available frequency band, as would be the case for larger organisms, or if a larger bandwidth had been available.

Inferences of microstructure parameters from measured broadband spectra

A least-squares inversion of the broadband acoustic-scattering data from the Kelvin–Helmholtz shear instability imaged on 14 August 2006 (region 2 in Figure 7a and b) was performed to determine the dissipation rate of turbulent kinetic energy, ε (W kg^{-1}), and temperature variance, χ_T (m^2 s^{-1}). The scattering model used is described in Lavery *et al.* (2007), and depth-averaged values for all model parameters, except ε and χ_T, were obtained from the direct microstructure data. The scattering is most sensitive to changes in ε and χ_T (because of the strong temperature gradients). The dissipation rate of salinity variance, χ_S, was set by using the temperature and salinity gradients measured by the direct microstructure profiler. The result of this inversion indicates that $\varepsilon = 8 \times 10^{-6}$ W kg^{-1} and $\chi_T = 3 \times 10^{-3}$ m^2 s^{-1}, in reasonable agreement with observed values (Figure 11a). In this particular example, the direct microstructure instrument happened to profile through the Kelvin–Helmholtz shear instability a number of times (Figure 8, left column), allowing more meaningful comparisons between the directly measured and acoustically inferred microstructure parameters.

Similarly, a least-squares inversion of the broadband acoustic-scattering data from the thin scattering layer located a few metres below the seasonal thermocline for the non-linear internal waves imaged on 22 August 2006 (region 2 in Figure 7c and d) was performed. Only the part of the spectrum that was consistent with scattering dominated by microstructure was used for this inversion (the LOW and MID channels). The result of this inversion indicates that $\varepsilon = 2.5 \times 10^{-6}$ W kg^{-1} and $\chi_T = 3.5 \times 10^{-4}$ m^2 s^{-1}. In this example, the direct microstructure profiles were sufficiently sparse that this particular feature was not well sampled (Figure 8, right column). However, the inferred values are well within the range of values measured with the direct microstructure instrument (Figure 11b).

The acoustic sampling volume and the sampling volume of the direct microstructure instrument are not well matched because: (i) the acoustic data are averaged over 10 pings and 1 m vertically, whereas the microstructure data are averaged over 1 m vertically but represent a point measurement in the horizontal; (ii) there is an offset of approximately half a vessel length between the two instruments; (iii) the direct microstructure data are relatively sparse ($\sim$200 pings were collected for every microstructure profile). However, the inferred values are well within the range of values measured directly (Figure 11), adding confidence to the interpretation of the spectra.

The acoustic frequency at which the diffusive roll-off occurs in the scattered spectrum for turbulent temperature microstructure is determined by the dissipation rate of turbulent kinetic energy and not by the dissipation rate of temperature variance, whereas the overall scattering levels are determined by both parameters. Therefore, in much the same way that inversion of broadband acoustic data for the location the Rayleigh-to-geometric scattering transition provides a relatively accurate method for determining zooplankton size, inversion of broadband acoustic-scattering data for the location of the diffusive roll-off provides a relatively accurate method for determining the dissipation rate of turbulent kinetic energy. In fact, the most robust method for determining the dissipation rate of turbulent kinetic energy is to resolve the roll-off in both the temperature and salinity dissipation spectra. This requires that both are resolvable and sufficient bandwidth. In contrast, absolute scattering levels are subject to the vagaries of calibration and to uncertainties in obtaining coincident direct microstructure measurements. However, because of the restricted frequency band available, the inversion of the broadband data for the frequency at which the diffusive roll-off occurred in the scattered spectrum for turbulent temperature microstructure was not as robust as desired. Additional bandwidth may have helped to assess more accurately the contribution to scattering from zooplankton, and/or it may have allowed both the temperature and salinity diffusive roll-offs to be determined, which would more conclusively allow the dissipation rate of turbulent kinetic energy to be determined, as well as more conclusively categorizing the scattering as being attributable to turbulent microstructure.

Conclusions

In this study, a commercial high-frequency broadband scattering system has been adapted for measuring acoustic scattering from oceanic microstructure and zooplankton over a broad and almost continuous range of frequencies spanning the range 150–600 kHz. For this emerging broadband technology to be used more prevalently for the study of zooplankton and microstructure, in much the same way as narrowband systems are used, it is critical to have user-friendly commercially available systems with documented calibration protocols. Details of the system specifications and calibration procedures have been outlined and the system performance has been assessed. The system

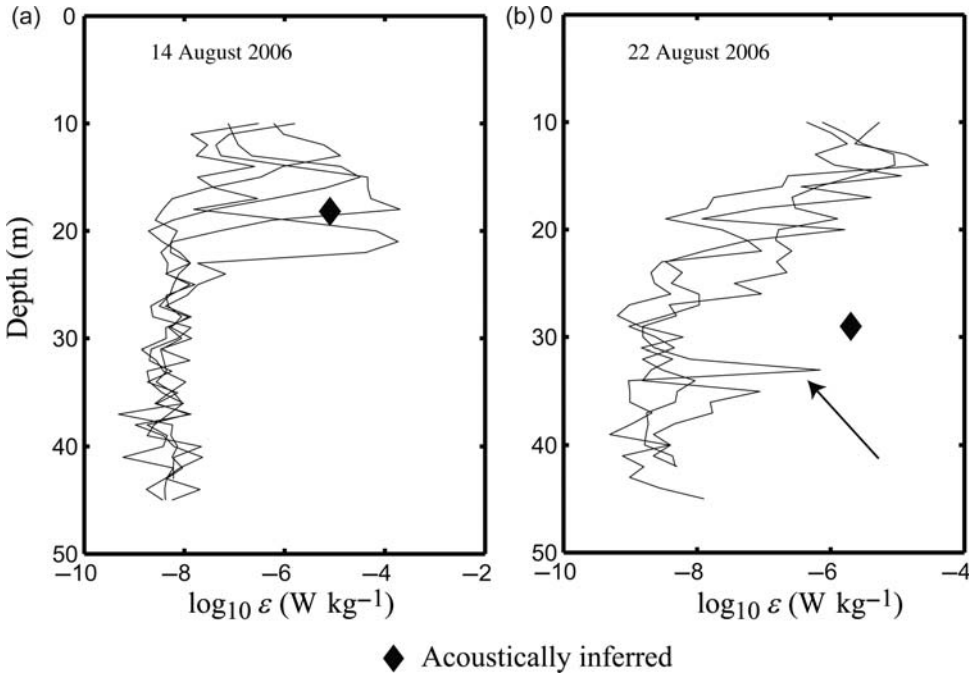

Figure 11. Dissipation rate of turbulent kinetic energy, ε (W kg^{-1}), on a log scale, as a function of depth and as measured by the direct microstructure profiler on (a) 14 August 2006 and (b) 22 August 2006, for the profiles indicated in Figure 8. The diamonds represent the acoustic inferences (regions 2 in Figure 7). The direct microstructure profiles sampled the Kelvin–Helmholtz instability imaged on 14 August 2006 (region 2 in Figure 7a and b) on various occasions, whereas the direct microstructure instrument did not sample region 2 in Figure 7c and d, attributed here to microstructure at LOW and MID frequencies, although it did sample a similar feature at a slightly different depth, indicated by the arrow.

has been deployed in regions of non-linear internal waves, where scattering from oceanic microstructure is expected to be enhanced relative to scattering of a biological origin. Coincident direct microstructure measurements were performed and zooplankton sampled using a depth-resolved net-sampling system.

The use of high-frequency broadband scattering techniques has resulted in the improvements listed below over either direct sampling techniques alone or the use of a small number of narrowband frequencies alone.

- *High-resolution imaging of oceanic microstructure*. Direct microstructure instruments provide very high-resolution measurements of certain parameters in the vertical direction, but other parameters, such as the dissipation rate of turbulent kinetic energy, can only be estimated in relatively coarse bins (typically bins of 0.5–1 m). Additionally, typical microstructure instruments are free-falling, and the profiling speed limits the horizontal resolution. The use of high-frequency broadband acoustic-scattering techniques allows very high-resolution measurements in range (or vertically for a downward-looking system) to be made, corresponding to various centimetres for the bandwidths in question, and also in the horizontal, because typical ping rates can be up to a few Hz, compared with microstructure instruments which profile every few minutes. Scattering features consistent with scattering from microstructure, such as Kelvin–Helmholtz shear instabilities, were observed using the broadband system during the passage of non-linear internal waves (region 2 of the non-linear internal wave sampled on 14 August 2006) that were not well resolved with the direct microstructure instrument.
- *Spectral discrimination*. The broadband scattering techniques allowed the spectra of different scattering features observed during the passage of non-linear internal waves to be measured. Spectra consistent with scattering dominated by temperature-dominated turbulent oceanic microstructure were observed, generally near shear instabilities (e.g. region 2 of the non-linear internal wave sampled on 14 August 2006), as well as spectra consistent with scattering dominated by small zooplankton (e.g. regions 1 of the non-linear internal waves sampled on 14 and 22 August 2006). Simple inversions of the acoustic data resulted in inferences of biological and physical parameters that were in reasonable agreement with the quantities measured directly, although the zooplankton ground-truthing was not temporally or spatially coincident. Many spectra were also observed that could not be interpreted confidently within the framework of the measured ground-truthing.
- *Simultaneous measurements of both zooplankton and microstructure on similar, and relevant, spatial and temporal scales*. Typical microstructure instruments do not have sensors appropriate for sampling zooplankton, and typical zooplankton net-sampling gear cannot measure microstructure adequately (because they are cabled). Therefore, simultaneous measurements of both zooplankton and microstructure are difficult to obtain using either microstructure instruments or net sampling systems. Broadband scattering spectra were measured in this study during the passage of a non-linear internal wave on 22 August 2006 (region 2) in which the scattering spectra were mixed, i.e. consistent with scattering dominated by microstructure at lower frequencies in the available band, and consistent with scattering dominated by small zooplankton at the higher frequencies of the available band. Although there are other possible scattering mechanisms that could, in principle, explain the mixed

spectra, the weight of evidence gathered, together with the simple inversions of the acoustic data resulting in reasonable parameter estimates, suggests that a mixture of zooplankton and microstructure are a likely mechanism. Therefore, broadband scattering techniques can result in the simultaneous observation and quantification of zooplankton and turbulence on similar and relevant spatial and temporal scales.

This work would have benefited from larger SNR and increased bandwidth. Increased bandwidth would have provided greater interpretive power. At the high frequency end, increased bandwidth would have allowed a more robust inversion for meaningful biological parameters for small zooplankton because the Rayleigh-to-geometric scattering transition for small zooplankton was at frequencies higher than the highest frequencies available (600 kHz). In addition, additional bandwidth at the high frequency end would have provided more confidence in the categorization of certain scattering features as being attributable to microstructure, particularly if the roll-off in both temperature and salinity dissipation spectra could be measured. Similarly, increased bandwidth at the lower frequency end would have allowed more robust classification of larger zooplankton because the Rayleigh-to-geometric scattering transition for larger zooplankton (e.g. euphausiids or amphipods) was at frequencies lower than the lowest frequency available (150 kHz). Increased bandwidth at the lower frequency end would also have allowed the contributions to scattering from bubbles to be assessed more confidently. Larger SNR would have allowed the effective range of the system to be increased, as well as allowing weaker scattering features to be characterized.

Notwithstanding, the results we have presented underscore the significant potential of high-frequency broadband acoustic-scattering techniques as an emerging technology for the detection and, under certain circumstances, quantification of oceanic microstructure and zooplankton. Although the study has stressed the benefits of broadband scattering techniques, it is also clear that appropriate ground-truthing remains central to the accurate interpretation of the scattering spectra.

Acknowledgements

We thank Karen Fisher, Paul Heslinga, and Doris Leong for helping collect the acoustic and MOCNESS data, Steve Wright and other EdgeTech employees for developing the system, Tim Stanton for assistance with system development and for loaning us his 1000-m coax cable, Mike Neeley-Brown and Ray Kreth for supporting OSU Ocean Mixing operations, John Kemp and his team, and the captain and crew of the RV "Oceanus". The work was supported by the US Office of Naval Research (Grant # N000140210359). Funding to pay the Open Access publication charges for this article was provided by the Ocean Acoustics Program of the US Office of Naval Research.

References

Atkins, P., Francis, D. T., and Foote, K. G. 2008. Calibration of broadband sonars using multiple standard targets. Journal of the Acoustical Society of America, 123: 3436. Also Proceedings of the Ninth European Conference on Underwater Acoustics, 1, pp. 261–266. Ed. by M. E. Zakharia, D. Cassereau, and F. Luppé. Société Française d'Acoustique, Paris.

Au, W. W. L., and Benoit-Bird, K. J. 2008. Broadband backscatter from individual Hawaiian mesopelagic boundary community animals with implications for spinner dolphin foraging. Journal of the Acoustical Society of America, 123: 2884–2894.

Au, W. W. L., Branstetter, B. K., Benoit-Bird, K. J., and Kastelein, R. A. 2009. Acoustic basis for fish prey discrimination by echolocating dolphins and porpoises. Journal of the Acoustical Society of America, 126: 460–467.

Benfield, M. C., Lavery, A. C., Wiebe, P. H., Greene, C. H., Stanton, T. K., and Copley, N. 2003. Distributions of physonect siphonulae in the Gulf of Maine and their potential as important sources of acoustic scattering. Canadian Journal of Fisheries and Aquatic Sciences, 60: 759–772.

Chu, D., and Stanton, T. K. 1998. Application of pulse compression techniques to broadband acoustic scattering by live individual zooplankton. Journal of the Acoustical Society of America, 104: 39–55.

Dragonette, L. R., Numrich, S. K., and Frank, L. J. 1981. Calibration technique for acoustic scattering measurements. Journal of the Acoustical Society of America, 69: 1186–1189.

Foote, K. G., Atkins, P. R., Francis, D. T. I., and Knutsen, T. 2005. Measuring echo spectra of marine organisms over a wide bandwidth. *In* Proceedings of the International Conference on Underwater Acoustic Measurements: Technologies and Results, II, Heraklion, Greece, 28 June–1 July 2005, pp. 501–508. Ed. by J. S. Papadakis, and L. Bjørnø. Institute of Applied and Computational Mathematics (IACM) at the Foundation for Research and Technology (FORTH), Hellas.

Foote, K. G., and MacLennan, D. N. 1984. Comparison of copper and tungsten carbide calibration spheres. Journal of the Acoustical Society of America, 75: 612–616.

Francois, R. E., and Garrison, G. R. 1982. Sound absorption based on ocean measurements. 2. Boric acid contribution and equation for total absorption. Journal of the Acoustical Society of America, 72: 1879–1890.

Goodman, L. 1990. Acoustic scattering from ocean microstructure. Journal of Geophysical Research, 95C: 11557–11573.

Holliday, D. V. 1972. Resonance structure in echoes from schooled pelagic fish. Journal of the Acoustical Society of America, 51: 1322–1332.

Holliday, D. V., and Pieper, R. E. 1995. Bioacoustical oceanography at high frequencies. ICES Journal of Marine Science, 52: 279–296.

Huntley, M. E., and Zhou, M. 2004. Influence of animals on turbulence in the sea. Marine Ecology Progress Series, 273: 65–79.

Kunze, E., Dower, J. F., Beveridge, I., Dewey, R., and Bartlett, K. P. 2006. Observations of biologically generated turbulence in a coastal inlet. Science, 313: 1768–1770.

Lavery, A. C., and Ross, T. 2007. Acoustic scattering from double-diffusive microstructure. Journal of the Acoustical Society of America, 122: 1449–1462.

Lavery, A. C., Schmitt, R. W., and Stanton, T. K. 2003. High-frequency acoustic scattering from turbulent oceanic microstructure: the importance of density fluctuations. Journal of the Acoustical Society of America, 114: 2685–2697.

Lavery, A. C., Wiebe, P. H., Stanton, T. K., Lawson, G., Benfield, M. C., and Copley, N. 2007. Determining dominant scatterers of sound in mixed zooplankton populations. Journal of the Acoustical Society of America, 122: 3304–3326.

Leong, D. 2009. Assessing the isotropy of ocean turbulence using broadband acoustics. MSc thesis, Dalhousie University, Canada. 60 pp.

Medwin, H. 1977. *In situ* acoustic measurements of microbubbles at sea. Journal of Geophysical Research, 82: 971–976.

Moum, J. N., Farmer, D. M., Smyth, W. D., Armi, L., and Vagle, S. 2003. Structure and generation of turbulence at interfaces strained by internal solitary waves propagation shoreward over the continental shelf. Journal of Physical Oceanography, 33: 2093–2122.

Moum, J. N., Gregg, M. C., Lien, R. C., and Carr, M. E. 1995. Comparison of turbulence kinetic energy dissipation rate estimates from two ocean microstructure profilers. Journal of Oceanic and Atmospheric Technology, 12: 346–366.

Napp, J. M., Ortner, P. B., Pieper, R. E., and Holliday, D. V. 1993. Biovolume-size spectra of epipelagic zooplankton using a Multi-frequency acoustic profiling system (MAPS). Deep Sea Research I, 40: 445–459.

Nicol, S., and Endo, Y. 1999. Krill fisheries: development, management and ecosystem implications. Aquatic Living Resources, 12: 105–120.

Oeschger, J., and Goodman, L. 2003. Acoustic scattering from a thermally driven buoyant plume revisited. Journal of the Acoustical Society of America, 113: 1353–1367.

Pieper, R. E., Holliday, D. V., and Kleppel, G. S. 1990. Quantitative zooplankton distributions from multifrequency acoustics. Journal of Plankton Research, 12: 433–441.

Roberts, P. L. D., and Jaffe, J. S. 2008. Classification of live, untethered zooplankton from observations of multiple-angle acoustic scatter. Journal of the Acoustical Society of America, 124: 796–802.

Ross, T., Gaboury, I., and Lueck, R. 2007. Simultaneous acoustic observations of turbulence and zooplankton in the ocean. Deep Sea Research I, 54: 143–153.

Ross, T., and Lawson, G. 2009. Long-term broadband acoustic observations of zooplankton scattering layers in Saanich Inlet, British Columbia. Journal of the Acoustical Society of America, 125: 2551.

Ross, T., and Lueck, R. 2003. Sound scattering from oceanic turbulence. Geophysical Research Letters, 30: 1343. doi:10.1029/2002GL016733.

Rothschild, B. J., and Osborn, T. R. 1988. Small-scale turbulence and plankton contact rates. Journal of Plankton Research, 10: 465–474.

Seim, H. E., Gregg, M. C., and Miyamoto, R. T. 1995. Acoustic backscatter from turbulent microstructure. Journal of Oceanic and Atmospheric Technology, 12: 367–380.

Seuront, L., Schmitt, F., and Lagadeuc, Y. 2001. Turbulence intermittency, small-scale phytoplankton patchiness and encounter rates in plankton: where do we go from here? Deep Sea Research I, 48: 1199–1215.

Simmonds, E. J., and MacLennan, D. N. 2005. Fisheries Acoustics, 2nd edn. Blackwell Publishing, Oxford. 437 pp.

Smyth, W. D., Moum, J. N., and Caldwell, D. R. 2001. The efficiency of mixing in turbulent patches: inferences from direct simulations and microstructure observations. Journal of Physical Oceanography, 31: 1969–1992.

Stanton, T. K., and Chu, D. 2008. Calibration of broadband active acoustic systems using a single standard spherical target. Journal of the Acoustical Society of America, 124: 128–136.

Stanton, T. K., Chu, D., and Jech, M. 2010. Resonance classification and high resolution imagery of swimbladder-bearing fish using a broadband echosounder. ICES Journal of Marine Science, 67: 000–000.

Stanton, T. K., Chu, D., and Wiebe, P. H. 1998b. Sound scattering by several zooplankton groups. 2. Scattering models. Journal of the Acoustical Society of America, 103: 236–253.

Stanton, T. K., Chu, D., Wiebe, P. H., Martin, L. V., and Eastwood, R. L. 1998a. Sound scattering by several zooplankton groups. 1. Experimental determination of dominant scattering mechanisms. Journal of the Acoustical Society of America, 103: 225–235.

Stanton, T. K., Wiebe, P. H., Chu, D., and Goodman, L. 1994. Acoustic characterization and discrimination of marine zooplankton and microstructure. ICES Journal of Marine Science, 51: 505–512.

Tang, D. J., Moum, J. N., Lynch, J., Abbot, P., Chapman, R., Dahl, P. H., Duda, T. F., *et al.* 2007. Shallow Water '06: a joint acoustic propagation/nonlinear internal wave physics experiment. Oceanography, 20: 156–158.

Thompson, C. H., and Love, R. H. 1996. Determination of fish size distributions and areal densities using broadband low-frequency measurements. ICES Journal of Marine Science, 53: 197–201.

Trevorrow, M. V., Mackas, D. L., and Benfield, M. C. 2005. Comparison of multi-frequency and *in situ* measurements of zooplankton abundances in Knight Inlet, British Columbia. Journal of the Acoustical Society of America, 117: 3574–3588.

Turin, G. L. 1960. An introduction to matched filters. IRE Transactions on Information Theory, IT-6: 311–329.

Urick, R. J. 1983. Principles of Underwater Sound, 3rd edn. McGraw-Hill, New York. 423 pp.

Van Trees, H. L. 1968. Detection, Estimation, and Modulation Theory. John Wiley, New York. 697 pp.

Warren, J. D., Stanton, T. K., Wiebe, P. H., and Seim, H. E. 2003. Inference of biological and physical parameters in an internal wave using multiple-frequency, acoustic-scattering data. ICES Journal of Marine Science, 60: 1033–1046.

Whalen, A. D. 1971. Detection of Signals in Noise. Academic Press, New York. 411 pp.

Wiebe, P. H., Grice, G. D., and Hoagland, E. 1973. Acid-iron waste as a factor affecting the distribution and abundance of zooplankton in the New York Bight. 2. Spatial variations in the field and implications for monitoring studies. Estuary and Coastal Shelf Science, 1: 51–64.

Wiebe, P. H., Morton, A. W., Bradley, A. M., Backus, R. H., Craddock, J. E., Barber, V., Cowles, T. J., *et al.* 1985. New developments in the MOCNESS, an apparatus for sampling zooplankton and micronekton. Marine Biology, 87: 313–323.

Wiebe, P. H., Stanton, T. K., Benfield, M., Mountain, D., and Greene, C. 1997. High frequency acoustic volume backscattering in the Georges Bank coastal region and its interpretation using scattering models. IEEE Journal of Oceanic Engineering, 22: 445–464.

Wishner, K. F., Schoenherr, J. R., Beardsley, R., and Chen, C. 1995. Abundance, distribution and population structure of the copepod *Calanus finmarchicus* in a springtime right whale feeding area in the southwestern Gulf of Maine. Continental Shelf Research, 15: 475–507.

Zakharia, M. E., Magand, F., Hetroit, F., and Diner, N. 1996. Wideband sounder for fish species identification at sea. ICES Journal of Marine Science, 53: 203–208.

doi:10.1093/icesjms/fsp242